

1

2 Modular strategies for spatial mapping of 3 diverse cell type data of the mouse brain

4 Nicholas J. Tustison¹, Min Chen², Fae N. Kronman³, Jeffrey T. Duda², Clare Gamlin⁴, Mia
5 G. Tustison, Michael Kunst⁴, Rachel Dalley⁴, Staci Sorenson⁴, Quanxin Wang⁴, Lydia Ng⁴,
6 Yongsoo Kim³, and James C. Gee²

7 ¹Department of Radiology and Medical Imaging, University of Virginia, Charlottesville, VA

8 ²Department of Radiology, University of Pennsylvania, Philadelphia, PA

9 ³Department of Neural and Behavioral Sciences, Penn State University, Hershey, PA

10 ⁴Allen Institute for Brain Science, Seattle, WA

11

12 Corresponding authors:

13

14 Nicholas J. Tustison, DSc

15 Department of Radiology and Medical Imaging

16 University of Virginia

17 ntustison@virginia.edu

18

19 James C. Gee, PhD

20 Department of Radiology

21 University of Pennsylvania

22 gee@upenn.edu

²³ **Abstract**

²⁴ Large-scale, international collaborative efforts by members of the BRAIN Initiative Cell
²⁵ Census Network (BICCN) consortium are aggregating the most comprehensive reference
²⁶ database to date for diverse cell type profiling of the mouse brain, which encompasses over
²⁷ 40 different multi-modal profiling techniques from more than 30 research groups. One cen-
²⁸ tral challenge for this integrative effort has been the need to map these unique datasets into
²⁹ common reference spaces such that the spatial, structural, and functional information from
³⁰ different cell types can be jointly analyzed. However, significant variation in the acquisition,
³¹ tissue processing, and imaging techniques across data types makes mapping such diverse
³² data a multifarious problem. Different data types exhibit unique tissue distortion and sig-
³³ nal characteristics that precludes a single mapping strategy from being generally applicable
³⁴ across all cell type data. Tailored mapping approaches are often needed to address the unique
³⁵ barriers present in each modality. This work highlights modular atlas mapping strategies
³⁶ developed across separate BICCN studies using the Advanced Normalization Tools Ecosys-
³⁷ tem (ANTsX) to map spatial transcriptomic (MERFISH) and high-resolution morphology
³⁸ (fMOST) mouse brain data into the Allen Common Coordinate Framework (AllenCCFv3),
³⁹ and developmental (MRI and LSFM) data into the Developmental Common Coordinate
⁴⁰ Framework (DevCCF). We discuss common mapping strategies that can be shared across
⁴¹ modalities and driven by specific challenges from each data type. These mapping strategies
⁴² include novel open-source contributions that are made publicly available through ANTSX.
⁴³ These include 1) a velocity flow-based approach for continuously mapping developmental
⁴⁴ trajectories such as that characterizing the DevCCF and 2) an automated framework for de-
⁴⁵ termining structural morphology solely through the leveraging of publicly resources. Finally,
⁴⁶ we provide general guidance to aid investigators to tailor these strategies to address unique
⁴⁷ data challenges without the need to develop additional specialized software.

⁴⁸ 1 Introduction

⁴⁹ Over the past decade there have been significant advancements in mesoscopic single-cell analysis of the mouse brain. It is now possible to track single neurons in mouse brains¹, observe whole brain developmental changes on a cellular level², associate brain regions and tissues with their genetic composition³, and locally characterize neural connectivity⁴. Much of these scientific achievements have been made possible due to breakthroughs in high resolution cell profiling and imaging techniques that permit submicron, multi-modal, 3-D characterizations of whole mouse brains. Among these include advanced techniques such as micro-optical sectioning tomography⁶, tissue clearing^{1,7}, spatial transcriptomics⁹, and single-cell genomic profiling¹⁰, which have greatly expanded the resolution and specificity of single-cell measurements in the brain.

⁵⁹ Recent efforts by the National Institutes of Health's Brain Research Through Advancing Innovative Neurotechnologies (BRAIN) Initiative has pushed for large-scale, international collaborative efforts to utilize these advanced single-cell techniques to create a comprehensive reference database for high-resolution transcriptomic, epigenomic, structural and imaging data of the mouse brain. This consortium of laboratories and data centers, known as the BRAIN Initiative Cell Census Network (BICCN), has archived datasets encompassing over 40 different multi-modal profiling techniques from more than 30 research groups, each providing unique characterizations of distinct cell types in the brain¹¹. Several of these modalities have been further developed into reference atlases to facilitate spatial alignment of individual brains and different data types into a common coordinate framework (CCF), thus allowing diverse single-cell information to be analyzed in an integrated manner. The most notable of these atlases is the Allen Mouse Brain Common Coordinate Framework (AllenCCFv3)¹², which serves as a primary target coordinate space for much of the work associated with the BICCN. Other atlases include modality-specific atlases^{13–15}, and spatiotemporal atlases^{16,17} for the developing mouse brain.

⁷⁴ **1.1 Mouse brain mapping**

⁷⁵ The cross-modality associations that can be learned from mapping different cell type data
⁷⁶ into a CCF is critical for improving our understanding of the complex relationships between
⁷⁷ cellular structure, morphology, and genetics in the brain. However, finding an accurate map-
⁷⁸ ping between each individual mouse brain and a CCF is a challenging and heterogeneous
⁷⁹ task. There is significant variance in the imaging protocols across different cell type data
⁸⁰ as well as different tissue processing and imaging methods which can potentially introduce
⁸¹ tissue distortion and signal differences^{18,19}. Certain modalities can have poor intensity corre-
⁸² spondence with the CCF, negatively impacting image alignment accuracy. Studies targeting
⁸³ specific regions or cell types can lead to missing anatomical correspondences. Other consid-
⁸⁴ erations include artifacts such as tissue distortion, holes, bubbles, folding, tears, and missing
⁸⁵ sections in the data that often require manual correction²⁰⁻²³. Given the diversity of these
⁸⁶ challenges, it is unlikely any single mapping approach can be generally applicable across all
⁸⁷ cell type data. Diverse, and often specialized, strategies are needed to address the unique
⁸⁸ barriers present for mapping each modality.

⁸⁹ Existing solutions to address mapping cell type data into the AllenCCFv3 falls broadly into
⁹⁰ three main categories. The first consists of integrated processing platforms that directly
⁹¹ provide mapped data to the users. These include the Allen Brain Cell Atlas²⁴ for the Allen
⁹² Reference Atlas (ARA) and associated data, the Brain Architecture Portal²⁵ for combined ex
⁹³ vivo radiology and histology data, OpenBrainMap²⁶ for connectivity data, and the Image and
⁹⁴ Multi-Morphology Pipeline²⁷ for high resolution morphology data. These platforms provide
⁹⁵ users online access to pre-processed, multi-modal cell type data that are already mapped to
⁹⁶ the AllenCCFv3. The platforms are designed such that the data is interactively manipulated
⁹⁷ by users through integrated visualization software that allow users to spatially manipulate
⁹⁸ and explore each dataset within the mapped space. While highly convenient for investigators
⁹⁹ who are interested in studying the specific modalities provided by these platforms, these
¹⁰⁰ systems can be limited in flexibility, general applicability, and public availability. As a
¹⁰¹ result, investigators often find it difficult to apply the same mapping solutions to their own
¹⁰² data.

103 The second category comprises specialized approaches specifically designed for mapping one
104 or more modalities into a CCF. These approaches use combinations of specialized manual and
105 automated processes that address specific challenges in each modality. Examples include ap-
106 proaches for mapping histology^{28–30}, magnetic resonance imaging (MRI)³⁷, micro-computed
107 tomography (microCT)^{35,37}, light-sheet fluorescence microscopy (LSFM)^{34,36–39}, fluorescence
108 micro-optical sectioning tomography (fMOST)^{15,40} and transcriptomic data^{41–43}. As special-
109 ized approaches, these techniques tend to boast higher mapping accuracy, robustness, and
110 ease of use. Conversely, their specialized designs often rely on base assumptions regard-
111 ing the data type that can make them rigid and difficult to adapt for new modalities or
112 unexpected artifacts and distortions in the data. Adapting these specialize software tools
113 to use with new data can require significant development, validation time, and engineering
114 expertise that may not be readily available for all investigators.

115 The last category consist of modular mapping approaches constructed using general im-
116 age analysis toolkits, which are software packages that include modular image processing,
117 segmentation and registration tools that have been previously developed, and validated for
118 multiple application areas. Examples of such toolkits include elastix⁴⁴, Slicer3D⁴⁵, ANTsX⁴⁶,
119 and several others which have all been applied towards mouse brain spatial mapping. The
120 main challenge, in these mouse-specific study scenarios, is that tailored pipelines often need
121 be constructed from available software components. Investigators must therefore be familiar
122 with the these tools for formulating new or adapting existing pipelines. However, in com-
123 parison to previously described specialized mapping approaches, these approaches are often
124 easier to create and prone to robustness, being typically constructed from pipeline compo-
125 nents which have been previously vetted in other contexts. In this work, we highlight such
126 mapping strategies designed using the ANTsX framework to map distinct mouse cell type
127 data with different characteristics into existing CCFs.

128 1.2 Advanced Normalization Tools (ANTsX)

129 The Advanced Normalization Tools Ecosystem (ANTsX) has been used in a number of
130 applications for mapping mouse brain data as part of core processing steps in various

¹³¹ workflows^{30,47–50}, particularly its pairwise, intensity-based image registration capabilities⁵¹
¹³² and bias field correction⁵². Historically, ANTsX development is originally based on fun-
¹³³ damental approaches to image mapping^{53–55}, particularly in the human brain, which has
¹³⁴ resulted in core contributions to the field such as the widely-used Symmetric Normalization
¹³⁵ (SyN) algorithm⁵¹. Since its development, various independent platforms have been used
¹³⁶ to evaluate ANTsX image registration capabilities in the context of different application
¹³⁷ foci which include multi-site brain MRI data⁵⁶, pulmonary CT data⁵⁷, and most recently,
¹³⁸ multi-modal brain registration in the presence of tumors⁵⁸.

¹³⁹ Apart from its registration capabilities, ANTsX comprises additional functionality such
¹⁴⁰ as template generation⁵⁹, intensity-based segmentation⁶⁰, preprocessing^{52,61}, deep learning
¹⁴¹ networks⁴⁶, and other utilities relevant to brain mapping (see Table 1). The use of the toolkit
¹⁴² has demonstrated high performance in multiple application areas (e.g., consensus labeling⁶²,
¹⁴³ brain tumor segmentation⁶³, and cardiac motion estimation⁶⁴). Importantly, ANTsX is built
¹⁴⁴ on the Insight Toolkit (ITK)⁶⁵ deriving benefit from the open-source community of scientists
¹⁴⁵ and programmers as well as providing an important resource for algorithmic development,
¹⁴⁶ evaluation, and improvement.

¹⁴⁷ With respect to mouse cell type data, ANTsX provides a comprehensive toolset which serves
¹⁴⁸ as a basis for developing modular frameworks for mapping diverse image data into com-
¹⁴⁹ mon coordinate frameworks (CCFs). Herein, we highlight its application for mapping data
¹⁵⁰ from separate BICCN projects focused on distinct data types: morphology data using flu-
¹⁵¹ orescence micro-optical sectioning tomography (fMOST), spatial transcriptomics from mul-
¹⁵² tiplexed error-robust fluorescence in situ hybridization (MERFISH) data, and time-series
¹⁵³ developmental data using light sheet fluorescence microscopy (LSFM) and magnetic reso-
¹⁵⁴ nance imaging (MRI). We describe both shared and targeted strategies developed to address
¹⁵⁵ the specific challenges of these modalities.

¹⁵⁶ 1.3 Novel ANTsX-based open-source contributions

¹⁵⁷ We introduce two novel inclusions to the ANTsX toolset that were developed as part of
¹⁵⁸ the MRI mapping and analysis pipeline for the Developmental Common Coordinate Frame-

¹⁵⁹ work (DevCCF). Consistent with previous ANTsX development, newly introduced capa-
¹⁶⁰ bilities introduced below are available through ANTsX (specifically, via R and Python
¹⁶¹ ANTsX packages), and illustrated through self-contained examples in the ANTsX tuto-
¹⁶² rial (<https://tinyurl.com/antsxtutorial>) with a dedicated GitHub repository specific to this
¹⁶³ work (<https://github.com/ntustison/ANTsXMouseBrainMapping>). To complement stan-
¹⁶⁴ dard preprocessing steps (e.g., bias correction, brain masking), additional mouse brain spe-
¹⁶⁵ cific tools have also been introduced to the ANTsX ecosystem, such as section reconstruction
¹⁶⁶ and landmark-based alignment with corresponding processing scripts (<https://github.com/>
¹⁶⁷ [dontminchenit/CCFAAlignmentToolkit](https://github.com/dontminchenit/CCFAAlignmentToolkit)).

¹⁶⁸ **1.3.1 Continuously mapping the DevCCF developmental trajectory with a ve-**
¹⁶⁹ **locity flow model**

¹⁷⁰ Recently, the Developmental Common Coordinate Framework (DevCCF) was introduced to
¹⁷¹ the mouse brain research community as a public resource¹⁶ comprising symmetric atlases of
¹⁷² multi-modal image data and anatomical segmentations defined by developmental ontology.
¹⁷³ These templates sample the mouse embryonic days E11.5, E13.5, E15.5, E18.5 and postnatal
¹⁷⁴ days P4, P14, and P56. Modalities include LSFM and at least four MRI contrasts per
¹⁷⁵ developmental stage. Anatomical parcellations are also available for each time point and
¹⁷⁶ were generated from ANTsX-based mappings of gene expression and other cell type data.
¹⁷⁷ Additionally, the P56 template was integrated with the AllenCCFv3 to further enhance the
¹⁷⁸ practical utility of the DevCCF. These processes, specifically template generation and multi-
¹⁷⁹ modal image mapping, were performed using ANTsX functionality in the presence of image
¹⁸⁰ mapping difficulties such as missing data and tissue distortion.

¹⁸¹ Given the temporal gaps in the discrete set of developmental atlases, we also provide an
¹⁸² open-source framework for inferring correspondence within the temporally continuous do-
¹⁸³ main sampled by the existing set of embryonic and postnatal atlases of the DevCCF. This
¹⁸⁴ recently developed functionality permits the generation of a diffeomorphic velocity flow trans-
¹⁸⁵ formation model⁶⁶, influenced by previous work⁶⁷. The resulting time-parameterized veloc-
¹⁸⁶ ity field spans the stages of the DevCCF where mappings between any two continuous time

¹⁸⁷ points within the span bounded by the E11.5 and P56 atlases are determined by numerical
¹⁸⁸ integration of the optimized velocity field.

¹⁸⁹ **1.3.2 Automated structural parcellations of the mouse brain**

¹⁹⁰ In contrast to the pipeline development in human data⁴⁶, limited tools exist yet to cre-
¹⁹¹ ate adequate training data for automated parcellations of the mouse brain. In addition,
¹⁹² mouse brain data acquisition often has unique issues, such as lower data quality or sampling
¹⁹³ anisotropy which limits its applicability to high resolution resources (e.g., AllenCCFv3, De-
¹⁹⁴ vCCF), specifically with respect to the corresponding granular brain parcellations derived
¹⁹⁵ from numerous hours of expert annotation leveraging multi-modal imaging resources.

¹⁹⁶ Herein, we introduce a mouse brain parcellation pipeline for multi-modal MRI comprising
¹⁹⁷ two novel deep learning components: two-shot learning brain extraction from data augmen-
¹⁹⁸ tation of two ANTsX templates generated from two open datasets^{68,69} and single-shot brain
¹⁹⁹ parcellation derived from the AllenCCFv3 labelings mapped to the corresponding DevCCF
²⁰⁰ P56 template.

²⁰¹ Although we anticipate that this pipeline will be beneficial to the research community, this
²⁰² work demonstrates more generally how one can leverage ANTsX tools and other public
²⁰³ resources for developing quantitative mouse brain morphological tools. Evaluation is per-
²⁰⁴ formed on an independent open dataset⁷⁰ comprising longitudinal acquisitions of multiple
²⁰⁵ specimens.

206 **2 Results**

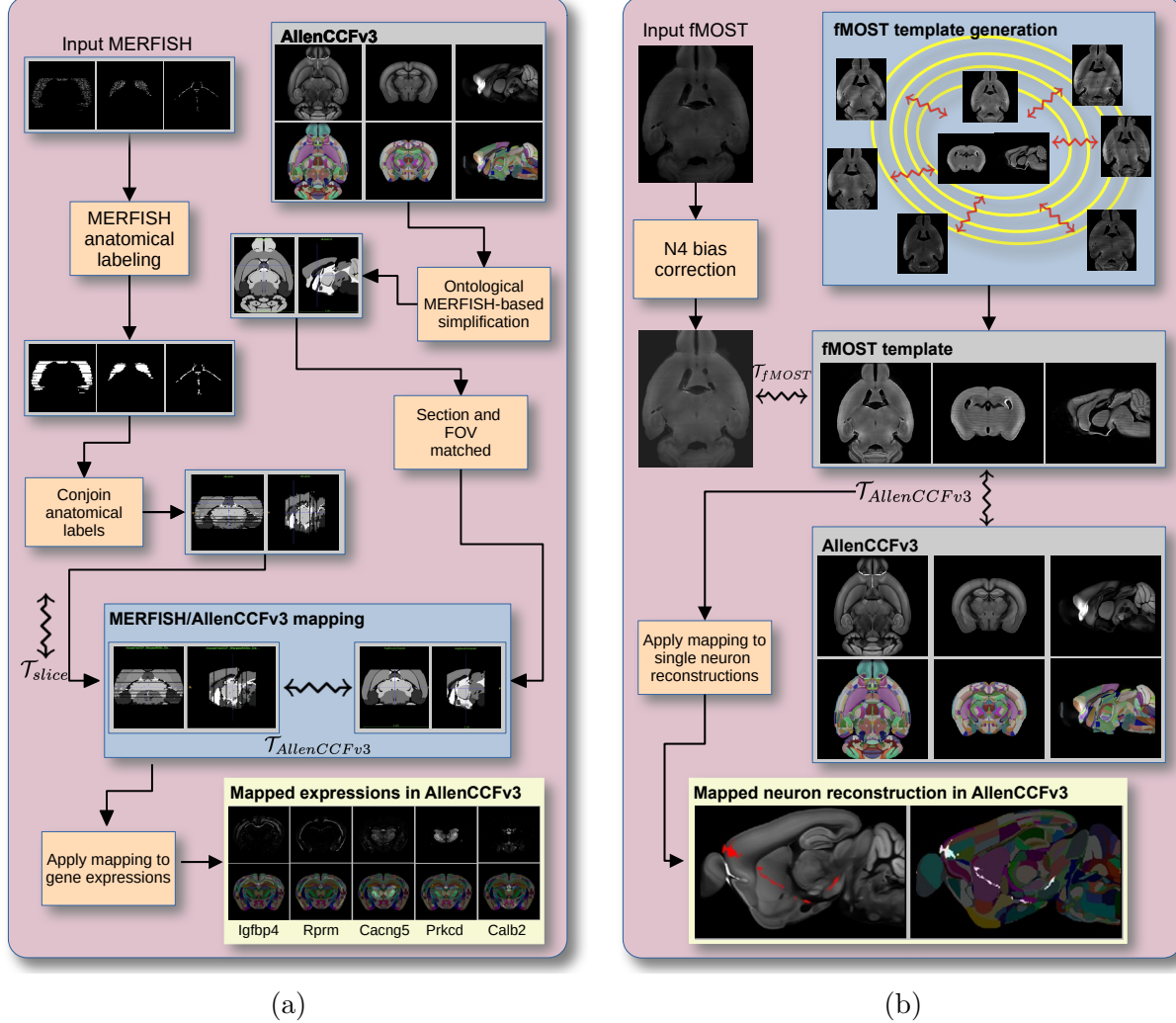


Figure 1: Diagram of the two ANTsX-based pipelines for mapping (a) MERFISH and (b)fMOST data into the space of AllenCCFv3. Each generates the requisite transforms, \mathcal{T} , to map individual images to the CCF.

207 **2.1 AllenCCFv3 brain image mapping**

208 **2.1.1 Mapping multiplexed error-robust fluorescence *in situ* hybridization
209 (MERFISH) data**

210 **Overview.** The ANTsX framework was used to develop a pipeline for mapping multiplexed
211 error-robust fluorescence *in situ* hybridization (MERFISH) spatial transcriptomic mouse

212 data onto the AllenCCFv3 (see Figure 1(a)). This pipeline, used recently in creating a
213 high-resolution transcriptomic atlas of the mouse brain⁵⁰, performs mappings by first gen-
214 erating anatomical labels from tissue related gene expressions in the MERFISH data, and
215 then spatially matching these labels to corresponding anatomical tissue parcellations in the
216 AllenCCFv3. The pipeline consists of MERFISH data specific preprocessing which includes
217 section reconstruction, mapping corresponding anatomical labels between AllenCCFv3 and
218 the spatial transcriptomic maps of the MERFISH data, and matching MERFISH sections
219 to the atlas space. Following preprocessing, two main alignment steps were performed: 1)
220 3-D global affine mapping and section matching of the AllenCCFv3 into the MERFISH data
221 and 2) 2-D global and deformable mapping between each MERFISH section and matched
222 AllenCCFv3 section. Mappings learned via each step in the pipeline are preserved and con-
223 catenated to provide point-to-point correspondence between the original MERFISH data
224 and AllenCCFv3, thus allowing individual gene expressions to be transferred into the Al-
225 lenCCFv3.

226 **Data.** MERFISH mouse brain data was acquired using a previously detailed procedure⁵⁰.
227 Briefly, a brain of C57BL/6 mouse was dissected according to standard procedures and
228 placed into an optimal cutting temperature (OCT) compound (Sakura FineTek 4583) in
229 which it was stored at -80°C. The fresh frozen brain was sectioned at 10 μm on Leica 3050
230 S cryostats at intervals of 200 μm to evenly cover the brain. A set of 500 genes were imaged
231 that had been carefully chosen to distinguish the ~5200 clusters of our existing RNAseq
232 taxonomy. For staining the tissue with MERFISH probes, a modified version of instructions
233 provided by the manufacturer was used⁵⁰. Raw MERSCOPE data were decoded using
234 Vizgen software (v231). Cells were segmented based on DAPI and PolyT staining using
235 Cellpose^{71,72}. Segmentation was performed on a median z-plane (fourth out of seven) and
236 cell borders were propagated to z-planes above and below. To assign cluster identity to each
237 cell in the MERFISH dataset, we mapped the MERFISH cells to the scRNA-seq reference
238 taxonomy.

239 **Evaluation.** Alignment of the MERFISH data into the AllenCCFv3 was qualitatively as-
240 sessed by an expert anatomist at each iteration of the registration using known correspon-

²⁴¹ dence of gene markers and their associations with the AllenCCFv3. As previously reported⁵⁰,
²⁴² further assessment of the alignment showed that, of the 554 terminal regions (gray matter
²⁴³ only) in the AllenCCFv3, only seven small subregions were missed from the MERFISH
²⁴⁴ dataset: frontal pole, layer 1 (FRP1), FRP2/3, FRP5; accessory olfactory bulb, glomerular
²⁴⁵ layer (AOBgl); accessory olfactory bulb, granular layer (AOBgr); accessory olfactory bulb,
²⁴⁶ mitral layer (AOBmi); and accessory supraoptic group (ASO).

²⁴⁷ 2.1.2 Mapping fluorescence micro-optical sectioning tomography (fMOST) data

²⁴⁸ **Overview.** We developed a pipeline for mapping fluorescence micro-optical sectioning to-
²⁴⁹ mography (fMOST) mouse brain images into the AllenCCFv3 (see Figure 1(b)). The pipeline
²⁵⁰ is adapted from previously developed frameworks for human brain mapping⁵⁹, and uses a
²⁵¹ modality specific (fMOST) average atlas to assist in the image registration and mapping.
²⁵² This approach has been well validated in human studies^{73–75}, and successfully used in other
²⁵³ mouse data^{12,15,34}. Briefly, we construct an intensity- and shape-based average fMOST atlas
²⁵⁴ using 30 fMOST images to serve as an intermediate registration target for mapping fMOST
²⁵⁵ images from individual specimens into the AllenCCFv3. Preprocessing steps include down-
²⁵⁶ sampling to match the $25\mu m$ isotropic AllenCCFv3, acquisition-based stripe artifact removal,
²⁵⁷ and inhomogeneity correction⁵². Preprocessing also includes a single annotation-driven reg-
²⁵⁸ istration to establish a canonical mapping between the fMOST atlas and the AllenCCFv3.
²⁵⁹ This step allows us to align expert determined landmarks to accurately map structures
²⁶⁰ with large morphological differences between the modalities, which are difficult to address
²⁶¹ using standard approaches. Once this canonical mapping is established, standard intensity-
²⁶² based registration is used to align each new fMOST image to the fMOST specific atlas.
²⁶³ This mapping is concatenated with the canonical fMOST atlas-to-AllenCCFv3 mapping to
²⁶⁴ further map each individual brain into the latter without the need to generate additional
²⁶⁵ landmarks. Transformations learned through this mapping can be applied to single neuron
²⁶⁶ reconstructions from the fMOST images to evaluate neuronal distributions across different
²⁶⁷ specimens into the AllenCCFv3 for the purpose of cell census analyses.

²⁶⁸ **Data.** The high-throughput and high-resolution fluorescence micro-optical sectioning to-

269 mography (fMOST)^{76,77} platform was used to image 55 mouse brains containing gene-defined
270 neuron populations, with sparse transgenic expression^{78,79}. In short, the fMOST imaging
271 platform results in 3-D images with voxel sizes of $0.35 \times 0.35 \times 1.0 \mu\text{m}^3$ and is a two-channel
272 imaging system where the green channel displays the green fluorescent protein (GFP) labeled
273 neuron morphology and the red channel is used to visualize the counterstained propidium
274 iodide cytoarchitecture. The spatial normalizations described in this work were performed
275 using the red channel, which offered higher tissue contrast for alignment, although other
276 approaches are possible including multi-channel registration.

277 **Evaluation.** Evaluation of the canonical fMOST atlas to Allen CCFv3 mapping was per-
278 formed via quantitative comparison at each step of the registration and qualitative assess-
279 ment of structural correspondence after alignment by an expert anatomist. Dice values were
280 generated for the following structures: whole brain, 0.99; fimbria, 0.91; habenular com-
281 missure, 0.63; posterior choroid plexus, 0.93; anterior choroid plexus, 0.96; optic chiasm,
282 0.77; caudate putamen, 0.97. Similar qualitative assessment was performed for each fMOST
283 specimen including the corresponding neuron reconstruction data.

284 2.2 Continuously mapping the DevCCF developmental trajectory 285 with a velocity flow model

286 The DevCCF is an openly accessible resource for the mouse brain research community¹⁶. It
287 consists of multi-modal MRI and LSFM symmetric ANTsX-generated templates⁵⁹ sampling
288 the mouse brain developmental trajectory, specifically the embryonic (E) and postnatal (P)
289 days E11.5, E13.5, E15.5, E18.5 P4, P14, and P56. Each template space includes structural
290 labels defined by a developmental ontology. Its utility is also enhanced by a coordinated
291 construction with AllenCCFv3. Although this work represents a significant contribution,
292 the gaps between time points potentially limit its applicability which could be addressed
293 through the development of the ability to map not only between time points but also within
294 and across time points.

295 To continuously generate transformations between the different stages of the DevCCF atlases,

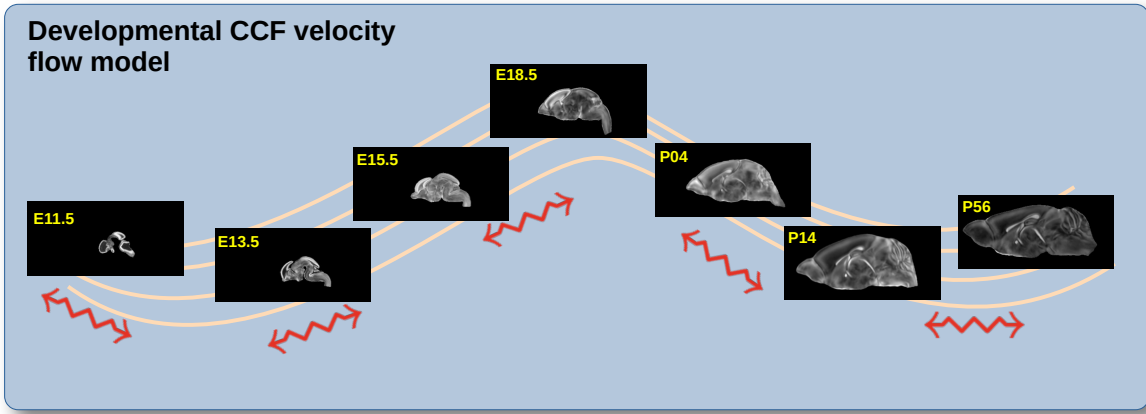


Figure 2: The spatial transformation between any two time points within the continuous DevCCF longitudinal developmental trajectory is available through the use of ANTsX functionality for generating a velocity flow model.

we developed a general velocity flow model approach which we apply to DevCCF-derived data. We also introduce this functionality into both the ANTsR and ANTsPy packages (for the latter, see `ants.fit_time_varying_transform_to_point_sets(...)`) for potential application to this and other analogous scenarios (e.g., modeling the cardiac and respiratory cycles). ANTsX, being built on top of ITK, uses an ITK image data structure for the 4-D velocity field where each voxel contains the x , y , z components of the field at that point.

2.2.1 Data

Labeled annotations are available as part of the original DevCCF and reside in the space of each developmental template which range in resolution from $31.5 - 50\mu\text{m}$. Across all atlases, the total number of labeled regions exceeds 2500. From these labels, a common set of 26 labels (13 per hemisphere) across all atlases were used for optimization and evaluation. These simplified regions include: terminal hypothalamus, subpallium, pallium, peduncular hypothalamus, prosomere, prosomere, prosomere, midbrain, prepontine hindbrain, pontine hindbrain, pontomedullary hindbrain, medullary hindbrain, and tracts (see Figure 3).

Prior to velocity field optimization, all data were rigidly transformed to DevCCF P56 using the centroids of the common label sets. In order to determine the landmark correspondence

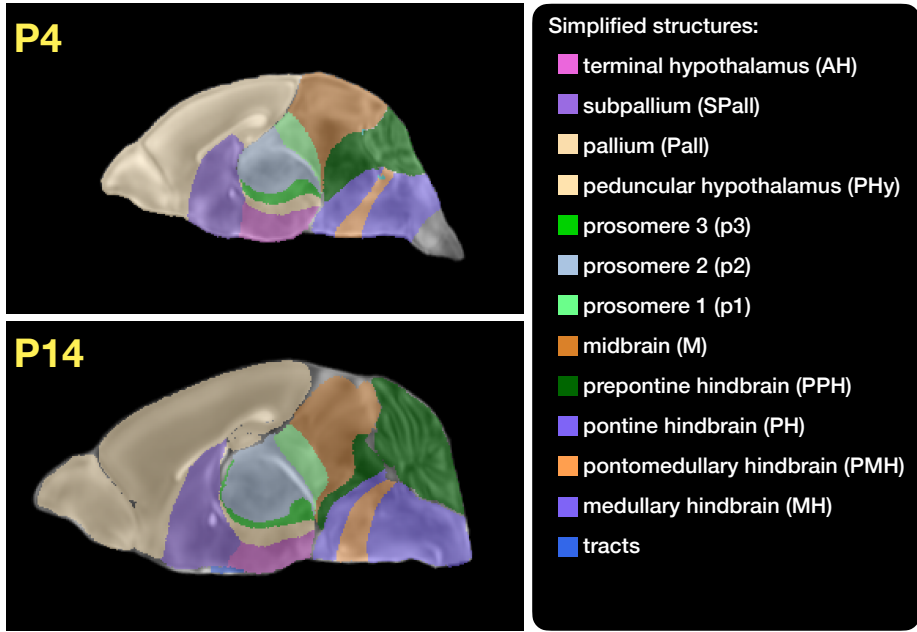


Figure 3: Annotated regions representing common labels across developmental stages which are illustrated for both P4 and P14.

312 across DevCCF stages, the multi-metric capabilities of `ants.registration(...)` were used.
 313 Instead of performing intensity-based pairwise registration directly on these multi-label im-
 314 ages, each label was used to construct a separate fixed and moving image pair resulting in a
 315 multi-metric registration optimization scenario involving 24 binary image pairs (each label
 316 weighted equally) for optimizing diffeomorphic correspondence between neighboring time
 317 point atlases using the mean squares metric and the symmetric normalization transform⁵¹.
 318 To generate the set of common point sets across all seven developmental atlases, the label
 319 boundaries and whole regions were sampled in the P56 atlas and then propagated to each
 320 atlas using the transformations derived from the pairwise registrations. We selected a sam-
 321 pling rate of 10% for the contour points and 1% for the regional points for a total number
 322 of points being per atlas being 173303 ($N_{contour} = 98151$ and $N_{region} = 75152$). Regional
 323 boundary points were weighted twice as those of non-boundary points during optimization.

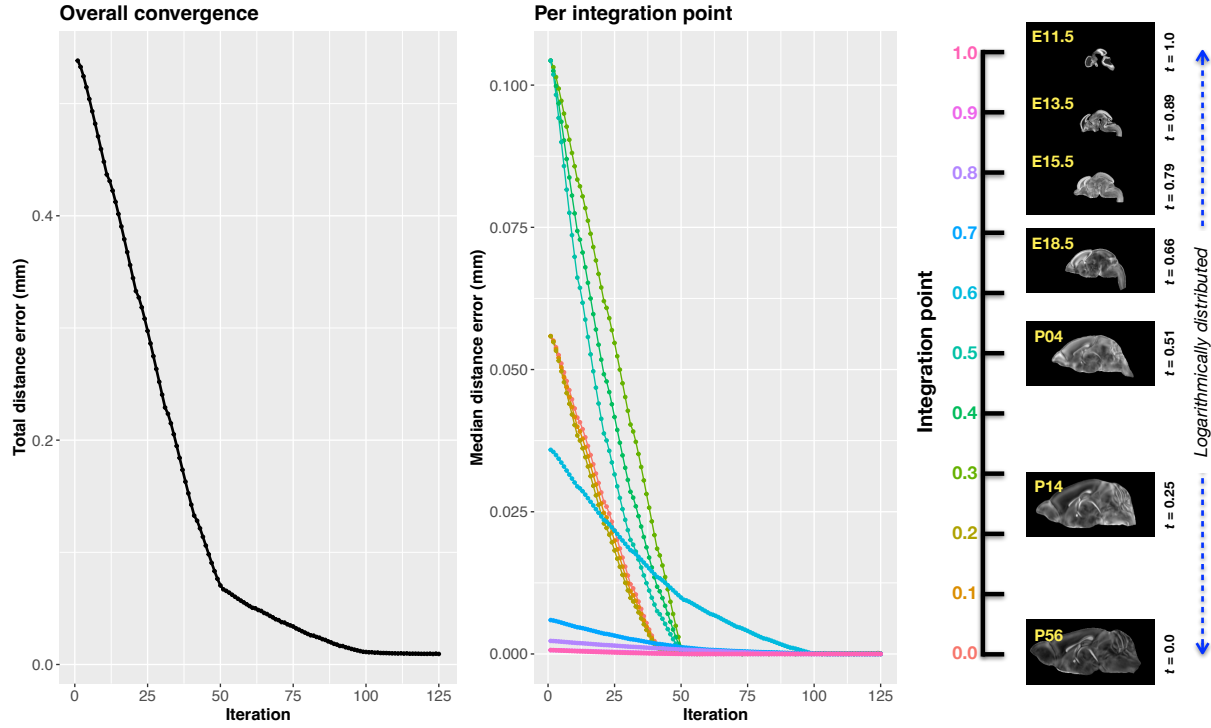


Figure 4: Convergence of the optimization of the velocity field for describing the transformation through the developmental stages from E11.5 through P56. Integration points in diagram on the right are color-coordinated with the center plot and placed in relation to the logarithmically situated temporal placement of the individual DevCCF atlases.

³²⁴ 2.2.2 Velocity field optimization

³²⁵ The velocity field was optimized using the input composed of the seven corresponding point
³²⁶ sets and their associated weight values, the selected number of integration points for the
³²⁷ velocity field ($N = 11$), and the parameters defining the geometry of the spatial dimensions
³²⁸ of the velocity field. Thus, the optimized velocity field described here is of size [256, 182, 360]
³²⁹ ($50\mu\text{m}$ isotropic) $\times 11$ integration points for a total compressed size of a little over 2 GB.

³³⁰ This choice represented weighing the trade-off between tractability, portability, and accuracy.
³³¹ However, all data and code to reproduce the results described are available in the dedicated
³³² GitHub repository.

³³³ The normalized time point scalar value for each atlas/point-set in the temporal domains $[0, 1]$
³³⁴ was also defined. Given the increasingly larger gaps in the postnatal time point sampling,
³³⁵ we made two adjustments. Based on known mouse brain development, we used 28 days for

336 the P56 data. We then computed the log transform of the adjusted set of time points prior
337 to normalization between 0 and 1 (see the right side of Figure 4). This log transform, as
338 part of the temporal normalization, significantly improves the temporal spacing of data.

339 The maximum number of iterations was set to 200 with each iteration taking approximately
340 six minutes on a 2020 iMac (processor, 3.6 GHz 10-Core Intel Core i9; memory, 64 GB 2667
341 MHz DDR4) At each iteration we looped over the 11 integration points. At each integration
342 point, the velocity field estimate was updated by warping the two immediately adjacent
343 point sets to the integration time point and determining the regularized displacement field
344 between the two warped point sets. As with any gradient-based descent algorithm, this field
345 was multiplied by a small step size ($\delta = 0.2$) before adding to the current velocity field.
346 Convergence is determined by the average displacement error over each of the integration
347 points. As can be seen in the left panel of Figure 4, convergence occurred around 125
348 iterations when the average displacement error over all integration points is minimized. The
349 median displacement error at each of the integration points also trends towards zero but at
350 different rates.

351 2.2.3 The velocity flow transformation model

352 Once optimized, the resulting velocity field can be used to generate the deformable transform
353 between any two continuous points within the time interval bounded by E11.5 and P56. As
354 a demonstration, in Figure 5, we transform each atlas to the space of every other atlas
355 using the DevCCF transform model. Additionally, one can use this transformation model
356 to construct virtual templates in the temporal gaps of the DevCCF. Given an arbitrarily
357 chosen time point within the normalized time point interval, the existing adjacent DevCCF
358 atlases on either chronological side can be warped to the desired time point. A subsequent
359 call to one of the ANTsX template building functions then permits the construction of the
360 template at that time point. In Figure 6, we illustrate the use of the DevCCF velocity flow
361 model for generating two such virtual templates for two arbitrary time points. Note that
362 both of these usage examples can be found in the GitHub repository previously given.

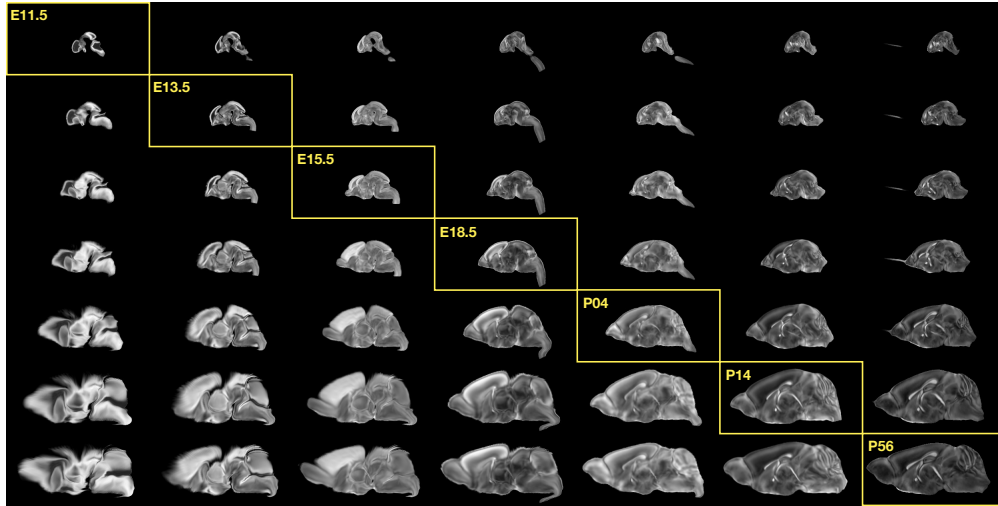


Figure 5: Mid-sagittal visualization of the effects of the transformation model in warping every developmental stage to the time point of every other developmental stage. The original images are located along the diagonal. Columns correspond to the warped original image whereas the rows represent the reference space to which each image is warped.

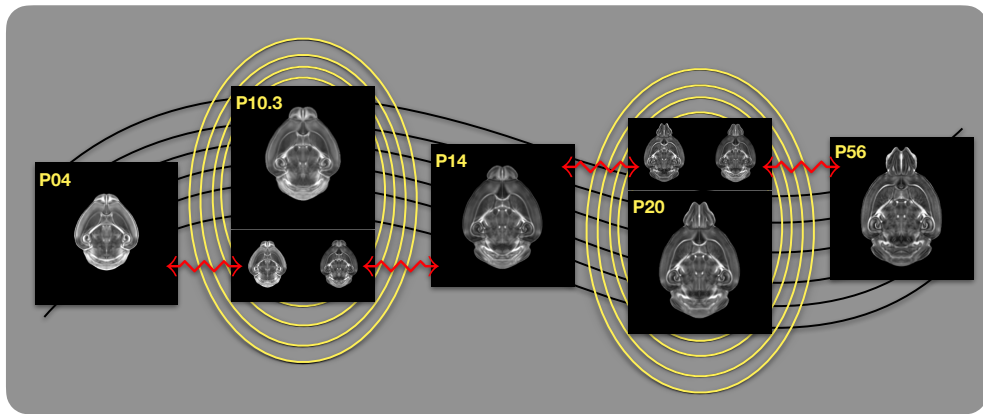


Figure 6: Illustration of the use of the velocity flow model for creating virtual templates at continuous time points not represented in one of the existing DevCCF time points. For example, FA templates at time point P10.3 and P20 can be generated by warping the existing temporally adjacent developmental templates to the target time point and using those images in the ANTsX template building process.

363 2.3 Automated structural parcellations of the mouse brain

364 Brain parcellation strategies for the mouse brain are pivotal for understanding the complex
365 organization and function of murine nervous system⁸⁰. By dividing the brain into distinct
366 regions based on anatomical, physiological, or functional characteristics, researchers can
367 investigate specific areas in isolation and identify their roles in various behaviors and pro-

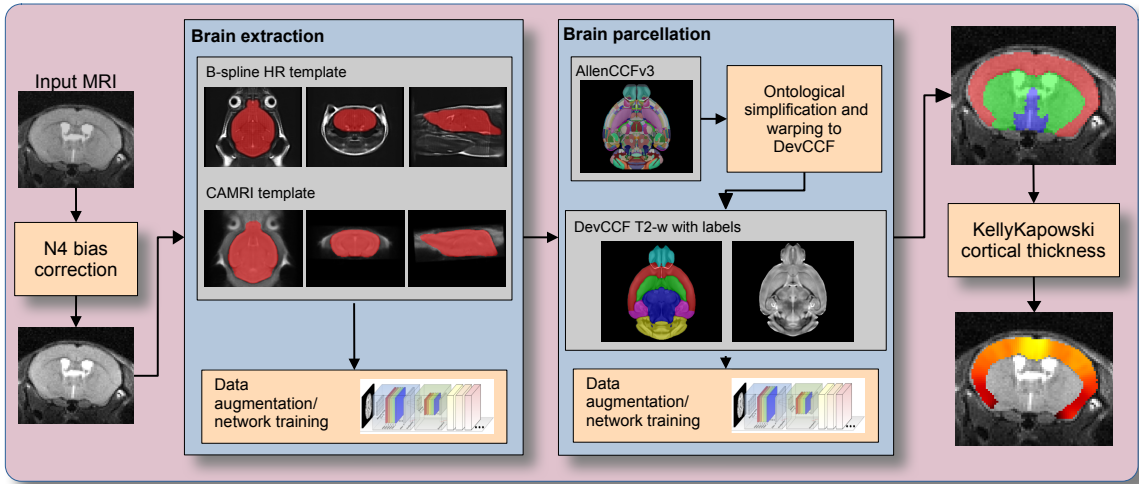


Figure 7: The mouse brain cortical parcellation pipeline integrating two deep learning components for brain extraction and brain parcellation prior to estimating cortical labels. Both deep learning networks rely heavily on aggressive data augmentation on templates built from open data and provide an outline for further refinement and creating alternative parcellations for tailored research objectives. Possible applications include voxelwise cortical thickness measurements.

cesses. For example, such parcellation schemes can help elucidate the spatial distribution of gene expression patterns⁸¹ as well as identify functional regions involved in specific cognitive tasks⁸².

Although deep learning techniques have been used to develop useful parcellation tools for human brain research (e.g., SynthSeg⁸³, ANTsXNet⁴⁶), analogous development for the mouse brain is limited. In addition, mouse data is often characterized by unique imaging issues such as extreme anisotropic sampling which are often in sharp contrast to the high resolution template-based resources available within the community, e.g., AllenCCFv3 and DevCCF. We demonstrate how one can use the ANTsX tools to develop a complete mouse brain structural morphology pipeline as illustrated in Figure 7 and detailed below.

2.3.1 Two-shot mouse brain extraction network

In order to create a generalized mouse brain extraction network, we built whole-head templates from two publicly available datasets. The Center for Animal MRI (CAMRI) dataset⁶⁸ from the University of North Carolina at Chapel Hill consists of 16 T2-w MRI volumes of

³⁸² voxel resolution $0.16 \times 0.16 \times 0.16\text{mm}^3$. The second high-resolution dataset⁶⁹ comprises
³⁸³ 88 specimens each with three spatially aligned canonical views with in-plane resolution of
³⁸⁴ $0.08 \times 0.08\text{mm}^2$ with a slice thickness of 0.5mm . These three orthogonal views were used
³⁸⁵ to reconstruct a single high-resolution volume per subject using a B-spline fitting algorithm
³⁸⁶ available in ANTsX⁸⁴. From these two datasets, two symmetric isotropic ANTsX templates⁵⁹
³⁸⁷ were generated analogous to the publicly available ANTsX human brain templates used in
³⁸⁸ previous research⁸⁵. Bias field simulation, intensity histogram warping, noise simulation,
³⁸⁹ random translation and warping, and random anisotropic resampling in the three canonical
³⁹⁰ directions were used for data augmentation in training a T2-w brain extraction network.

³⁹¹ 2.3.2 Single-shot mouse brain parcellation network

³⁹² AllenCCFv3 and its hierarchical ontological labeling, along with the DevCCF, provides the
³⁹³ necessary data for developing a tailored structural parcellation network for multi-modal
³⁹⁴ imaging. The `allensdk` Python library permits the creation of any gross parcellation based
³⁹⁵ on the AllenCCFv3 ontology. For example, using `allensdk` we coalesced the labels to the
³⁹⁶ following six major structures: cerebral cortex, cerebral nuclei, brain stem, cerebellum, main
³⁹⁷ olfactory bulb, and hippocampal formation. This labeling was mapped to the P56 component
³⁹⁸ of the DevCCF for use with the T2-w template component. Both the T2-w P56 DevCCF
³⁹⁹ and labelings, in conjunction with the data augmentation described previously for brain
⁴⁰⁰ extraction, were used to train the proposed brain parcellation network. Note that other
⁴⁰¹ brain parcellation networks have also been trained using alternative regions and parcellation
⁴⁰² schemes and are available in the same ANTsXNet functionality.

⁴⁰³ 2.3.3 Evaluation

⁴⁰⁴ Although the utility of the proposed brain parcellation framework is highly dependent on
⁴⁰⁵ the specific application, we demonstrate the utility through the generation of cortical thick-
⁴⁰⁶ ness maps⁸⁶ which leverages both brain parcellation and the capabilities of mouse brain-
⁴⁰⁷ based isotropic interpolation for anisotropic data. Cortical thickness has demonstrated util-
⁴⁰⁸ ity in both human (e.g.,^{85,87}) and non-human data (e.g., canines⁸⁸, dolphins⁸⁹, non-human

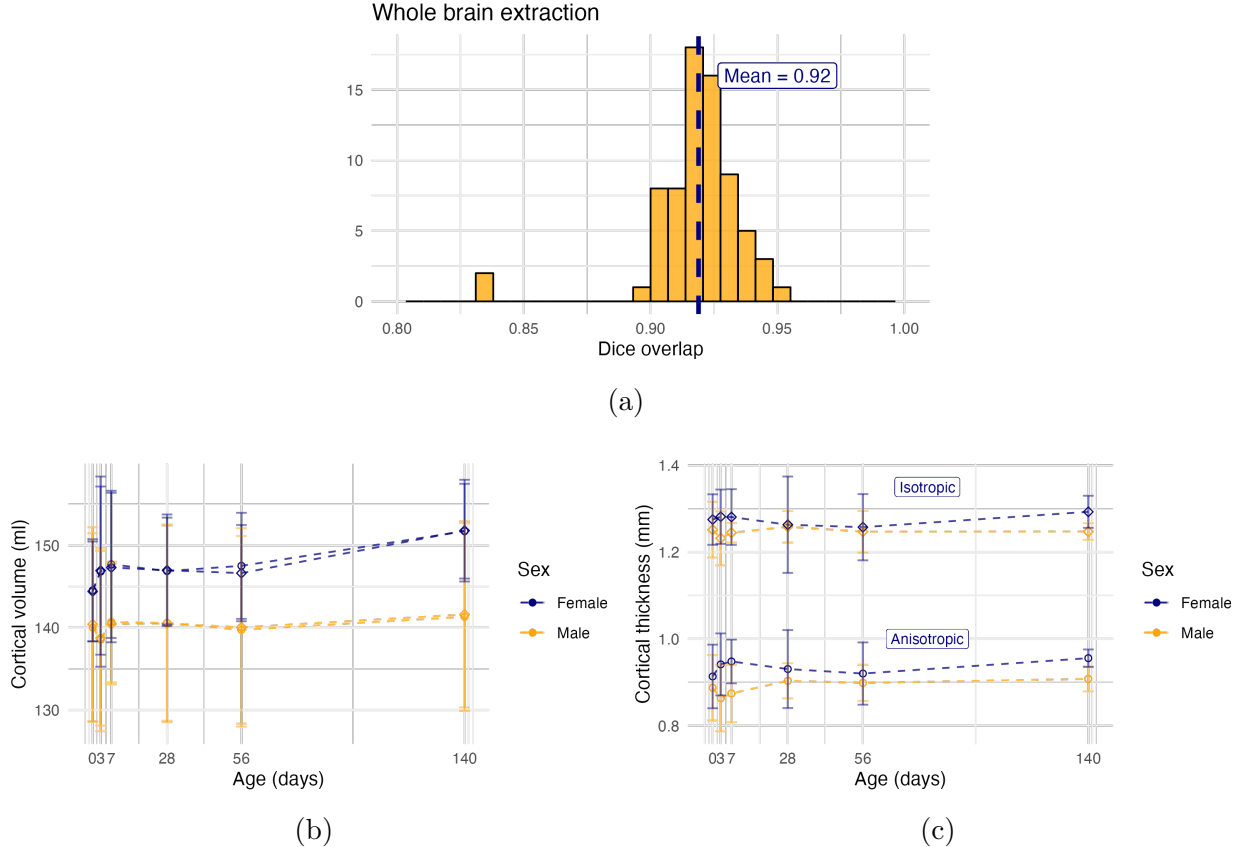


Figure 8: Evaluation of the ANTsX mouse brain extraction, parcellation, and cortical thickness pipeline on an independent dataset consisting of 12 specimens \times 7 time points = 84 total images. (a) Dice overlap comparisons with the user-generated brain masks provide good agreement with the automated results from the brain extraction network. (b) Cortical volume measurements show similar average quantities over growth and development between the original anisotropic data and interpolated isotropic data. (c) The volumetric comparative results contrast with the cortical thickness measurements which illustrate estimation in anisotropic space severely underestimates the actual values in comparison with the isotropic prediction.

⁴⁰⁹ primates⁹⁰) including the mouse brain^{41,91–93}.

⁴¹⁰ For evaluation, we used an additional publicly available dataset⁷⁰ which is completely inde-
⁴¹¹ pendent from the data used in training the brain extraction and parcellation networks. Data
⁴¹² includes 12 specimens each imaged at seven time points (Day 0, Day 3, Week 1, Week 4, Week
⁴¹³ 8, Week 20) with in-house-generated brain masks. Spacing is anisotropic with an in-plane
⁴¹⁴ resolution of $0.1 \times 0.1 mm^2$ and a slice thickness of $0.5 mm$. Since the training data is isotropic
⁴¹⁵ and data augmentation includes downsampling in the canonical directions, each of the two
⁴¹⁶ networks learns mouse brain-specific interpolation such that one can perform prediction on
⁴¹⁷ thick-sliced images, as, for example, in these evaluation data, and return isotropic probabil-
⁴¹⁸ ity and thickness maps (a choice available to the user). Figure 8 summarizes the results of
⁴¹⁹ the evaluation and comparison between isotropic and anisotropic cortical measurements in
⁴²⁰ male and female specimens.

421 **3 Discussion**

422 The diverse mouse brain cell type profiles gathered through BICCN and associated efforts
423 provides a rich multi-modal resource to the research community. However, despite significant
424 progress, optimized leveraging of these valuable resources is ongoing. A central component
425 to data integration is accurately mapping novel cell type data into CCFs for subsequent
426 processing and analysis. To meet these needs, tools for mapping mouse cell type data must
427 be both generally accessible to a wide audience of investigators, and capable of handling
428 distinct challenges unique to each data type. In this work, we described modular ANTsX-
429 based pipelines developed to address the needs of three BICCN projects that cover distinct
430 cell type data, including spatial transcriptomic, morphological, and developmental data. We
431 highlighted how a modular toolbox like ANTsX can be tailored to address problems unique
432 to each modality through leveraging a variety of ready-to-use powerful tools that have been
433 previously validated in multiple application scenarios.

434 Our MERFISH pipeline provides an example of how to map high-resolution spatial transcripto-
435 mic data into the AllenCCFv3. While the techniques employed for mapping the sectioned
436 data can be generally applicable to spatially transform other serial histology images, much
437 of the pipeline was designed to specifically address known alignment challenges in the MER-
438 FISH data. Thus pipeline shows how general ANTsX tools can be adapted to target highly
439 specialized problems in mouse cell type data.

440 In contrast to the MERFISH pipeline, our fMOST pipeline was designed to be a more general
441 solution that can be employed in other modalities. The pipeline primarily uses previously
442 developed ANTsX preprocessing and atlasing tools to map fMOST data into the AllenCCFv3.
443 The key component of the pipeline is the use of a fMOST-specific average shape and intensity
444 atlas to most effectively address image registration in this context. The mapping between
445 the fMOST atlas is generated once and reused for each new fMOST image. Lastly, ANTsX
446 provides point set transformation tools to allow the mappings found through the pipeline to
447 be directly applied to associated single-cell reconstructions from the fMOST data to study
448 neuronal morphology.

449 The pipeline for continuously mapping the DevCCF data is also available in ANTsX and
450 is generally applicable for spatio-temporal mapping. With specific application to the De-
451 vCCF, despite the significant expansion of available developmental age templates beyond
452 what existed previously, there are still temporal gaps in the DevCCF which can be poten-
453 tially sampled by future research efforts. However, pioneering work involving time-varying
454 diffeomorphic transformations allow us to continuously situate the existing templates within
455 a velocity flow model. This allows one to determine the diffeomorphic transformation from
456 any one temporal location to any other temporal location within the time span defined by
457 the temporal limits of the DevCCF. This functionality is built on multiple ITK components
458 including the B-spline scattered data approximation technique for field regularization and
459 velocity field integration. This velocity field model permits intra-template comparison and
460 the construction of virtual templates where a template can be estimated at any continuous
461 time point within the temporal domain. This novel application can potentially enhance our
462 understanding of intermediate developmental stages.

463 We also presented a mouse brain morphological pipeline for brain extraction and brain
464 parcellation using single-shot and two-shot learning with data augmentation. This approach
465 attempts to circumvent (or at least minimize) the typical requirement of large training
466 datasets as with the human ANTsX pipeline analog. However, even given our initial success
467 on independent data, we anticipate that refinements will be necessary. Given that the ANTsX
468 toolkit is a dynamic effort undergoing continual improvement, we manually correct cases that
469 fail and use them for future training and refinement of network weights as we have done for
470 our human-based networks. Generally, these approaches provide a way to bootstrap training
471 data for manual refinement and future generation of more accurate deep learning networks
472 in the absence of other applicable tools.

473 The ANTsX ecosystem is a powerful framework that has demonstrated applicability to di-
474 verse cell type data in the mouse brain. This is further evidenced by the many software
475 packages that use various ANTsX components in their own mouse-specific workflows. The
476 extensive functionality of ANTsX makes it possible to create complete processing pipelines
477 without requiring the integration of multiple packages or lengthy software development.

⁴⁷⁸ These open-source components not only perform well but are available across multiple plat-
⁴⁷⁹ forms which facilitates the construction of tailored pipelines for individual study solutions.
⁴⁸⁰ These components are also supported by years of development not only by the ANTsX
⁴⁸¹ development team but by the larger ITK community.

482 **4 Methods**

483 The following methods are all available as part of the ANTsX ecosystem with analogous
484 elements existing in both ANTsR (ANTs in R) and ANTsPy (ANTs in Python) with an
485 ANTs/ITK C++ core. However, most of the development for the work described below was
486 performed using ANTsPy. For equivalent calls in ANTsR, please see the ANTsX tutorial at
487 <https://tinyurl.com/antsxtutorial>.

488 **4.1 General ANTsX utilities**

489 Although they focus on distinct data types, the three pipelines presented share common
490 components that are generally applicable when mapping mouse cell type data. These include,
491 addressing intensity biases and noise in the data, image registration to solve the mapping,
492 creating custom templates and atlases from the data, and visualization of the results. Table
493 1 provides a brief summary of key general functionalities in ANTsX for addressing these
494 challenges.

495 **4.1.1 Preprocessing: bias field correction and denoising**

496 Bias field correction and image denoising are standard preprocessing steps in improving over-
497 all image quality in mouse brain images. The bias field, a gradual spatial intensity variation
498 in images, can arise from various sources such as magnetic field inhomogeneity or acquisition
499 artifacts, leading to distortions that can compromise the quality of brain images. Correct-
500 ing for bias fields ensures a more uniform and consistent representation of brain structures,
501 enabling more accurate quantitative analysis. Additionally, brain images are often suscep-
502 tible to various forms of noise, which can obscure subtle features and affect the precision
503 of measurements. Denoising techniques help mitigate the impact of noise, enhancing the
504 signal-to-noise ratio and improving the overall image quality. The well-known N4 bias field
505 correction algorithm⁵² has its origins in the ANTs toolkit which was implemented and intro-
506 duced into the ITK toolkit, i.e. `ants.n4_bias_field_correction(...)`. Similarly, ANTsX

Table 1: Sampling of ANTsX functionality

<i>ANTsPy: Preprocessing</i>	
bias field correction	<code>n4_bias_field_correction(...)</code>
image denoising	<code>denoise_image(...)</code>
<i>ANTsPy: Registration</i>	
image registration	<code>registration(...)</code>
image transformation	<code>apply_transforms(...)</code>
template generation	<code>build_template(...)</code>
landmark registration	<code>fit_transform_to_paired_points(...)</code>
time-varying landmark reg.	<code>fit_time_varying_transform_to_point_sets(...)</code>
integrate velocity field	<code>integrate_velocity_field(...)</code>
invert displacement field	<code>invert_displacement_field(...)</code>
<i>ANTsPy: Segmentation</i>	
MRF-based segmentation	<code>atropos(...)</code>
Joint label fusion	<code>joint_label_fusion(...)</code>
diffeomorphic thickness	<code>kelly_kapowski(...)</code>
<i>ANTsPy: Miscellaneous</i>	
Regional intensity statistics	<code>label_stats(...)</code>
Regional shape measures	<code>label_geometry_measures(...)</code>
B-spline approximation	<code>fit_bspline_object_to_scattered_data(...)</code>
Visualize images and overlays	<code>plot(...)</code>
<i>ANTsPyNet: Mouse-specific</i>	
brain extraction	<code>mouse_brain_extraction(...modality="t2"...)</code>
brain parcellation	<code>mouse_brain_parcellation(...)</code>
cortical thickness	<code>mouse_cortical_thickness(...)</code>
super resolution	<code>mouse_histology_super_resolution(...)</code>

ANTsX provides state-of-the-art functionality for processing biomedical image data. Such tools, including deep learning networks, support a variety of mapping-related tasks. A more comprehensive listing of ANTsX tools with self-contained R and Python examples is provided as a gist page on GitHub (<https://tinyurl.com/antsxtutorial>).

507 contains an implementation of a well-performing patch-based denoising technique⁶¹ and is
508 also available as an image filter to the ITK community, `ants.denoise_image(...)`.

509 **4.1.2 Image registration**

510 The ANTs registration toolkit is a complex framework permitting highly tailored solutions
511 to pairwise image registration scenarios⁹⁴. It includes innovative transformation models
512 for biological modeling^{51,67} and has proven capable of excellent performance^{56,95}. Vari-
513 ous parameter sets targeting specific applications have been packaged with the different
514 ANTsX packages, specifically ANTs, ANTsPy, and ANTsR⁴⁶. In ANTsPy, the function
515 `ants.registration(...)` is used to register a pair of images or a pair of image sets where
516 `type_of_transform` is a user-specified option that invokes a specific parameter set. For ex-
517 ample `type_of_transform='antsRegistrationSyNQuick[s]'` encapsulates an oft-used pa-
518 rameter set for quick registration whereas `type_of_transform='antsRegistrationSyN[s]'`
519 is a more aggressive alternative. Transforming images using the derived transforms is per-
520 formed via the `ants.apply_transforms(...)` function.

521 Initially, linear optimization is initialized with center of (intensity) mass alignment typically
522 followed by optimization of both rigid and affine transforms using the mutual information
523 similarity metric. This is followed by diffeomorphic deformable alignment using symmetric
524 normalization (SyN) with Gaussian⁵¹ or B-spline regularization⁶⁷ where the forward trans-
525 form is invertible and differentiable. The similarity metric employed at this latter stage is
526 typically either neighborhood cross-correlation or mutual information. Note that these pa-
527 rameter sets are robust to input image type (e.g., light sheet fluorescence microscopy, Nissl
528 staining, and the various MRI modalities) and are adaptable to mouse image geometry and
529 scaling. Further details can be found in the various documentation sources for these ANTsX
530 packages.

531 **4.1.3 Template generation**

532 ANTsX provides functionality for constructing templates from a set (or multi-modal sets) of
533 input images as originally described⁵⁹ and recently used to create the DevCCF templates¹⁶.

534 An initial template estimate is constructed from an existing subject image or a voxelwise
535 average derived from a rigid pre-alignment of the image population. Pairwise registration
536 between each subject and the current template estimate is performed using the Symmetric
537 Normalization (SyN) algorithm⁵¹. The template estimate is updated by warping all subjects
538 to the space of the template, performing a voxelwise average, and then performing a “shape
539 update” of this latter image by warping it by the average inverse deformation, thus yielding
540 a mean image of the population in terms of both intensity and shape. The corresponding
541 ANTsPy function is `ants.build_template(...)`.

542 4.1.4 Visualization

543 To complement the well-known visualization capabilities of R and Python, e.g., `ggplot2`
544 and `matplotlib`, respectively, image-specific visualization capabilities are available in the
545 `ants.plot(...)` function (Python). These are capable of illustrating multiple slices in
546 different orientations with other image overlays and label images.

547 4.2 Mapping fMOST data to AllenCCFv3

548 4.2.1 Preprocessing

- 549 • *Downsampling*. The first challenge when mapping fMOST images into the AllenCCFv3
550 is addressing the resolution scale of the data. Native fMOST data from an individual
551 specimen can range in the order of terabytes, which leads to two main problems. First,
552 volumetric registration methods (particularly those estimating local deformation) have
553 high computational complexity and typically cannot operate on such high-resolution
554 data under reasonable memory and runtime constraints. Second, the resolution of
555 the AllenCCFv3 atlas is much lower than the fMOST data, thus the mapping process
556 will cause much of the high-resolution information in the fMOST images to be lost
557 regardless. Thus, we perform a cubic B-spline downsampling of the fMOST data to
558 reduce the resolution of each image to match the isotropic $25 \mu\text{m}$ voxel resolution of the
559 AllenCCFv3 intensity atlas using `ants.resample_image(...)`. An important detail

560 to note is that while the fMOST images and atlas are downsampled, the mapping
561 learned during the registration is assumed to be continuous. Thus, after establishing
562 the mapping to the AllenCCFv3, we can interpolate the learned mapping and apply it
563 directly to the high-resolution native data directly to transform any spatially aligned
564 data (such as the single-cell neuron reconstructions) into the AllenCCFv3.

- 565 • *Stripe artifact removal.* Repetitive pattern artifacts are a common challenge in fMOST
566 imaging where inhomogeneity during the cutting and imaging of different sections can
567 leave stripes of hyper- and hypo-intensity across the image. These stripe artifacts
568 can be latched onto by the registration algorithm as unintended features that are
569 then misregistered to non-analogous structures in the AllenCCFv3. We address these
570 artifacts by fitting a 3-D bandstop (notch) filter to target the frequency of the stripe
571 patterns and removing them prior to the image registration.
- 572 • *Inhomogeneity correction.* Regional intensity inhomogeneity can also occur within
573 and between sections in fMOST imaging due to staining or lighting irregularity during
574 acquisition. Similar to stripe artifacts, intensity gradients due to inhomogeneity
575 can be misconstrued as features during the mapping and result in matching of non-
576 corresponding structures. Our pipeline addresses these intensity inhomogeneities using
577 N4 bias field correction⁵², `ants.n4_bias_field_correction(...)`.

578 4.2.2 Steps for spatial normalization to AllenCCFv3

- 579 1. *Average fMOST atlas as an intermediate target.* Due to the preparation of the mouse
580 brain for fMOST imaging, the resulting structure in the mouse brain has several large
581 morphological deviations from the AllenCCFv3 atlas. Most notable of these is an en-
582 largement of the ventricles, and compression of cortical structures. In addition, there is
583 poor intensity correspondence for the same anatomic features due to intensity dissim-
584 ilarity between imaging modalities. We have found that standard intensity-base reg-
585 istration is insufficient to capture the significant deformations required to map these
586 structures correctly into the AllenCCFv3. We address this challenge in ANTsX by
587 using explicitly corresponding parcellations of the brain, ventricles and surrounding

588 structures to directly recover these large morphological differences. However, generating
589 these parcellations for each individual mouse brain is a labor-intensive task. Our
590 solution is to create an average atlas whose mapping to AllenCCFv3 encapsulates these
591 large morphological differences to serve as an intermediate registration point. This has
592 the advantage of only needing to generate one set of corresponding annotations which
593 is used to register between the two atlas spaces. New images are first aligned to the
594 fMOST average atlas, which shares common intensity and morphological features and
595 thus can be achieved through standard intensity-based registration.

596 2. *Average fMOST atlas construction.* An intensity and shape-based contralaterally sym-
597 metric average of the fMOST image data is constructed from 30 images and their
598 contralateral flipped versions. We ran three iterations of the atlas construction using
599 the default settings. Additional iterations (up to six) were evaluated and showed mini-
600 mal changes to the final atlas construction, suggesting a convergence of the algorithm.

601 3. *fMOST atlas to AllenCCFv3 alignment.* Alignment between the fMOST average atlas
602 and AllenCCFv3 was performed using a one-time annotation-driven approach. Label-
603 to-label registration is used to align 7 corresponding annotations in both atlases in
604 the following: 1) brain mask/ventricles, 2) caudate/putamen, 3) fimbria, 4) posterior
605 choroid plexus, 5) optic chiasm, 6) anterior choroid plexus, and 7) habenular com-
606 missure. The alignments were performed sequentially, with the largest, most relevant
607 structures being aligned first using coarse registration parameters, followed by other
608 structures using finer parameters. This coarse-to-fine approach allows us to address
609 large morphological differences (such as brain shape and ventricle expansion) at the
610 start of registration and then progressively refine the mapping using the smaller struc-
611 tures. The overall ordering of these structures was determined manually by an expert
612 anatomist, where anatomical misregistration after each step of the registration was
613 evaluated and used to determine which structure should be used in the subsequent it-
614 eration to best improve the alignment. The transformation from this one-time expert-
615 guided alignment is preserved and used as the canonical fMOST atlas to AllenCCFv3
616 mapping in the pipeline.

- 617 4. *Alignment of individual fMOST mouse brains.* The canonical transformation between
618 the fMOST atlas and AllenCCFv3 greatly simplifies the registration of new individ-
619 ual fMOST mouse brains into the AllenCCFv3. Each new image is first registered
620 into the fMOST average atlas, which shares intensity, modality, and morphologi-
621 cal characteristics. This allows us to leverage standard, intensity-based registration
622 functionality⁹⁴ available in ANTsX to perform this alignment. Transformations are
623 then concatenated to the original fMOST image to move it into the AllenCCFv3 space
624 using `ants.apply_transforms(...)`.
- 625 5. *Transformation of single cell neurons.* A key feature of fMOST imaging is the ability
626 to reconstruct and examine whole-brain single neuron projections⁷⁹. Spatial mapping
627 of these neurons from individual brains into the AllenCCFv3 allows investigators to
628 study different neuron types within the same space and characterize their morphology
629 with respect to their transcriptomics. Mappings found between the fMOST image
630 and the AllenCCFv3 using our pipeline can be applied in this way to fMOST neuron
631 reconstruction point set data using `ants.apply_transforms_to_points(..)`.

632 **4.3 Mapping MERFISH data to AllenCCFv3**

633 **4.3.1 Preprocessing**

- 634 • *Initial volume reconstruction.* Alignment of MERFISH data into a 3-D atlas space
635 requires an estimation of anatomical structure within the data. For each section,
636 this anatomic reference image was created by aggregating the number of detected
637 genetic markers (across all probes) within each pixel of a $10 \times 10 \mu\text{m}^2$ grid to match
638 the resolution of the $10 \mu\text{m}$ AllenCCFv3 atlas. These reference image sections are then
639 coarsely reoriented and aligned across sections using manual annotations of the most
640 dorsal and ventral points of the midline. The procedure produces an anatomic image
641 stack that serves as an initialization for further global mappings into the AllenCCFv3.
- 642 • *Anatomical correspondence labeling.* Mapping the MERFISH data into the AllenCCFv3
643 requires us to establish correspondence between the anatomy depicted in the MERFISH

and AllenCCFv3 data. Intensity-based features in MERFISH data are not sufficiently apparent to establish this correspondence, so we need to generate instead corresponding anatomical labelings of both images with which to drive registration. These labels are already available as part of the AllenCCFv3; thus, the main challenge is deriving analogous labels from the spatial transcriptomic maps of the MERFISH data. Toward this end, we assigned each cell from the scRNA-seq dataset to one of the following major regions: cerebellum, CTXsp, hindbrain, HPF, hypothalamus, isocortex, LSX, midbrain, OLF, PAL, sAMY, STRd, STRv, thalamus and hindbrain. A label map of each section was generated for each region by aggregating the cells assigned to that region within a $10 \times 10\mu m^2$ grid. The same approach was used to generate more fine grained region specific landmarks (i.e., cortical layers, habenula, IC). Unlike the broad labels which cover large swaths of the section these regions are highly specific to certain parts of the section. Once cells in the MERFISH data are labeled, morphological dilation is used to provide full regional labels for alignment into the AllenCCFv3.

- *Section matching.* Since the MERFISH data is acquired as sections, its 3-D orientation may not be fully accounted for during the volume reconstruction step, due to the particular cutting angle. This can lead to obliqueness artifacts in the section where certain structures can appear to be larger or smaller, or missing outright from the section. To address this, we first use a global alignment to match the orientations of the MERFISH sections to the atlas space. In our pipeline, this section matching is performed in the reverse direction by performing a global affine transformation of the AllenCCFv3 into the MERFISH data space, and then resampling digital sections from the AllenCCFv3 to match each MERFISH section. This approach limits the overall transformation and thus resampling that is applied to the MERFISH data, and, since the AllenCCFv3 is densely sampled, it also reduces in-plane artifacts that result from missing sections or undefined spacing in the MERFISH data.

670 **4.3.2 2.5D deformable, landmark-driven alignment to AllenCCFv3**

671 After global alignment of the AllenCCFv3 into the MERFISH dataset, 2D per-section de-
672 formable refinements are used to address local differences between the MERFISH sections
673 and the resampled AllenCCFv3 sections. Nine registrations were performed in sequence us-
674 ing a single label at each iteration in the following order: 1) brain mask, 2) isocortex (layer
675 2+3), 3) isocortex (layer 5), 4) isocortex (layer 6), 5) striatum, 6) medial habenula, 7) lateral
676 habenula, 8) thalamus, and 9) hippocampus. This ordering was determined empirically by
677 an expert anatomist who prioritized which structure to use in each iteration by evaluat-
678 ing the anatomical alignment from the previous iteration. Global and local mappings are
679 then all concatenated (with appropriate inversions) to create the final mapping between the
680 MERFISH data and AllenCCFv3. This mapping is then used to provide a point-to-point
681 correspondence between the original MERFISH coordinate space and the AllenCCFv3 space,
682 thus allowing mapping of individual genes and cell types located in the MERFISH data to
683 be directly mapped into the AllenCCFv3.

684 **4.4 DevCCF velocity flow transformation model**

685 Given multiple, linearly or non-linearly ordered point sets where individual points across the
686 sets are in one-to-one correspondence, we developed an approach for generating a velocity
687 flow transformation model to describe a time-varying diffeomorphic mapping as a variant of
688 the landmark matching solution. Integration of the resulting velocity field can then be used
689 to describe the displacement between any two time points within this time-parameterized
690 domain. Regularization of the sparse correspondence between point sets is performed using
691 a generalized B-spline scattered data approximation technique⁸⁴, also created by the ANTsX
692 developers and contributed to ITK.

693 **4.4.1 Velocity field optimization**

694 To apply this methodology to the developmental templates¹⁶, we coalesced the manual an-
695 notations of the developmental templates into 26 common anatomical regions (see Figure 3).

696 We then used these regions to generate invertible transformations between successive time
697 points. Specifically each label was used to create a pair of single region images resulting in 26
698 pairs of “source” and “target” images. The multiple image pairs were simultaneously used to
699 iteratively estimate a diffeomorphic pairwise transform. Given the seven atlases E11.5, E13.5,
700 E15.5, E18.5, P4, P14, and P56, this resulted in 6 sets of transforms between successive time
701 points. Approximately 10^6 points were randomly sampled labelwise in the P56 template
702 space and propagated to each successive atlas providing the point sets for constructing the
703 velocity flow model. Approximately 125 iterations resulted in a steady convergence based
704 on the average Euclidean norm between transformed point sets. Ten integration points were
705 used and point sets were distributed along the temporal dimension using a log transform for
706 a more evenly spaced sampling. For additional information a help menu is available for the
707 ANTsPy function `ants.fit_time_varying_transform_to_point_sets(...)`.

708 4.5 ANTsXNet mouse brain applications

709 4.5.1 General notes regarding deep learning training

710 All network-based approaches described below were implemented and organized in the
711 ANTsXNet libraries comprising Python (ANTsPyNet) and R (ANTsRNet) analogs using
712 the Keras/Tensorflow libraries available as open-source in ANTsX GitHub repositories.
713 For the various applications, both share the identically trained weights for mutual re-
714 producibility. For all GPU training, we used Python scripts for creating custom batch
715 generators which we maintain in a separate GitHub repository for public availability
716 (<https://github.com/ntustison/ANTsXNetTraining>). These scripts provide details such as
717 batch size, choice of loss function, and network parameters. In terms of GPU hardware, all
718 training was done on a DGX (GPUs: 4X Tesla V100, system memory: 256 GB LRDIMM
719 DDR4).

720 Data augmentation is crucial for generalizability and accuracy of the trained networks.
721 Intensity-based data augmentation consisted of randomly added noise (i.e., Gaussian, shot,
722 salt-and-pepper), simulated bias fields based on N4 bias field modeling, and histogram warp-

723 ing for mimicking well-known MRI intensity nonlinearities^{46,96}. These augmentation tech-
724 niques are available in ANTsXNet (only ANTsPyNet versions are listed with ANTsRNet
725 versions available) and include:

- 726 • image noise: `ants.add_noise_to_image(...)`,
- 727 • simulated bias field: `antspynet.simulate_bias_field(...)`, and
- 728 • nonlinear intensity warping: `antspynet.histogram_warp_image_intensities(...)`.

729 Shape-based data augmentation used both random linear and nonlinear deformations in
730 addition to anisotropic resampling in the three canonical orientations to mimic frequently
731 used acquisition protocols for mice brains:

- 732 • random spatial warping: `antspynet.randomly_transform_image_data(...)` and
- 733 • anisotropic resampling: `ants.resample_image(...)`.

734 4.5.2 Brain extraction

735 Similar to human neuroimage processing, brain extraction is a crucial preprocessing step
736 for accurate brain mapping. We developed similar functionality for T2-weighted mouse
737 brains. This network uses a conventional U-net architecture⁹⁷ and, in ANTsPyNet, this
738 functionality is available in the program `antspynet.mouse_brain_extraction(...)`.
739 For the two-shot T2-weighted brain extraction network, two brain templates were gen-
740 erated along with their masks. One of the templates was generated from orthogonal
741 multi-plane, high resolution data⁶⁹ which were combined to synthesize isotropic volu-
742 metric data using the B-spline fitting algorithm⁸⁴. This algorithm is encapsulated in
743 `ants.fit_bspline_object_to_scattered_data(...)` where the input is the set of voxel
744 intensity values and each associated physical location. Since each point can be assigned
745 a confidence weight, we use the normalized gradient value to more heavily weight edge
746 regions. Although both template/mask pairs are available in the GitHub repository
747 associated with this work, the synthesized volumetric B-spline T2-weighted pair is available
748 within ANTsXNet through the calls:

- 749 • template: `antspynet.get_antsxnet_data("bsplineT2MouseTemplate")` and
750 • mask: `antspynet.get_antsxnet_data("bsplineT2MouseTemplateBrainMask")`.

751 **4.5.3 Brain parcellation**

752 The T2-weighted brain parcellation network is also based on a 3-D U-net architecture and the
753 T2-w DevCCF P56 template component with extensive data augmentation, as described pre-
754 viously. Intensity differences between the template and any brain extracted input image are
755 minimized through the use of the rank intensity transform (`ants.rank_intensity(...)`).
756 Shape differences are reduced by the additional preprocessing step of warping the brain ex-
757 tracted input image to the template. Additional input channels include the prior probability
758 images created from the template parcellation. These images are also available through the
759 ANTsXNet `get_antsxnet_data(...)` interface.

760 **Data availability**

761 All data and software used in this work are publicly available. The DevCCF atlas is
762 available at <https://kimlab.io/brain-map/DevCCF/>. ANTsPy, ANTsR, ANTsPyNet, and
763 ANTsRNet are available through GitHub at the ANTsX Ecosystem ([https://github.com/](https://github.com/ANTsX)
764 [ANTsX](#)). Training scripts for all deep learning functionality in ANTsXNet can also be
765 found on GitHub (<https://github.com/ntustison/ANTsXNetTraining>). A GitHub reposi-
766 tory specifically pertaining to the AllenCCFv3 mapping is available at <https://github.com/>
767 [dontminchenit/CCFAAlignmentToolkit](#). For the other two contributions contained in this
768 work, the longitudinal DevCCF mapping and mouse cortical thickness pipeline, we refer the
769 interested reader to <https://github.com/ntustison/ANTsXMouseBrainMapping>.

⁷⁷⁰ **Acknowledgments**

⁷⁷¹ Support for the research reported in this work includes funding from the National Institute
⁷⁷² of Biomedical Imaging and Bioengineering (R01-EB031722) and National Institute of Mental
⁷⁷³ Health (RF1-MH124605 and U24-MH114827).

⁷⁷⁴ Author contributions

⁷⁷⁵ N.T., M.C., and J.G. wrote the main manuscript text and figures. M.C., M.K., R.D., S.S.,
⁷⁷⁶ Q.W., L.G., J.D., C.G., and J.G. developed the Allen registration pipelines. N.T. and F.K.
⁷⁷⁷ developed the time-varying velocity transformation model for the DevCCF. N.T. and M.T.
⁷⁷⁸ developed the brain parcellation and cortical thickness methodology. All authors reviewed
⁷⁷⁹ the manuscript.

780 **References**

- 781 1. Keller, P. J. & Ahrens, M. B. Visualizing whole-brain activity and development at
the single-cell level using light-sheet microscopy. *Neuron* **85**, 462–83 (2015).
- 782 2. La Manno, G. *et al.* Molecular architecture of the developing mouse brain. *Nature*
596, 92–96 (2021).
- 783 3. Wen, L. *et al.* Single-cell technologies: From research to application. *Innovation
(Camb)* **3**, 100342 (2022).
- 784 4. Oh, S. W. *et al.* A mesoscale connectome of the mouse brain. *Nature* **508**, 207–14
(2014).
- 785 5. Gong, H. *et al.* Continuously tracing brain-wide long-distance axonal projections in
mice at a one-micron voxel resolution. *Neuroimage* **74**, 87–98 (2013).
- 786 6. Li, A. *et al.* Micro-optical sectioning tomography to obtain a high-resolution atlas of
the mouse brain. *Science* **330**, 1404–8 (2010).
- 787 7. Ueda, H. R. *et al.* Tissue clearing and its applications in neuroscience. *Nat Rev
Neurosci* **21**, 61–79 (2020).
- 788 8. Ståhl, P. L. *et al.* Visualization and analysis of gene expression in tissue sections by
spatial transcriptomics. *Science* **353**, 78–82 (2016).
- 789 9. Burgess, D. J. Spatial transcriptomics coming of age. *Nat Rev Genet* **20**, 317 (2019).
- 790 10. Hardwick, S. A. *et al.* Single-nuclei isoform RNA sequencing unlocks barcoded exon
connectivity in frozen brain tissue. *Nature biotechnology* **40**, 1082–1092 (2022).
- 791 11. Hawrylycz, M. *et al.* A guide to the BRAIN initiative cell census network data
ecosystem. *PLoS biology* **21**, e3002133 (2023).
- 792 12. Wang, Q. *et al.* The allen mouse brain common coordinate framework: A 3D reference
atlas. *Cell* **181**, 936–953.e20 (2020).
- 793 13. Perens, J. *et al.* An optimized mouse brain atlas for automated mapping and quantification
of neuronal activity using iDISCO+ and light sheet fluorescence microscopy.
Neuroinformatics **19**, 433–446 (2021).
- 794 14. Ma, Y. *et al.* A three-dimensional digital atlas database of the adult C57BL/6J mouse
brain by magnetic resonance microscopy. *Neuroscience* **135**, 1203–1215 (2005).

- 795 15. Qu, L. *et al.* Cross-modal coherent registration of whole mouse brains. *Nature Methods* **19**, 111–118 (2022).
- 796 16. Kronman, F. A. *et al.* Developmental mouse brain common coordinate framework. *bioRxiv* (2023) doi:[10.1101/2023.09.14.557789](https://doi.org/10.1101/2023.09.14.557789).
- 797 17. Chuang, N. *et al.* An MRI-based atlas and database of the developing mouse brain. *Neuroimage* **54**, 80–89 (2011).
- 798 18. Dries, R. *et al.* Advances in spatial transcriptomic data analysis. *Genome research* **31**, 1706–1718 (2021).
- 799 19. Ricci, P. *et al.* Removing striping artifacts in light-sheet fluorescence microscopy: A review. *Progress in biophysics and molecular biology* **168**, 52–65 (2022).
- 800 20. Agarwal, N., Xu, X. & Gopi, M. Robust registration of mouse brain slices with severe histological artifacts. in *Proceedings of the tenth indian conference on computer vision, graphics and image processing* 1–8 (2016).
- 801 21. Agarwal, N., Xu, X. & Gopi, M. Automatic detection of histological artifacts in mouse brain slice images. in *Medical computer vision and bayesian and graphical models for biomedical imaging: MICCAI 2016 international workshops, MCV and BAMBI, athens, greece, october 21, 2016, revised selected papers* 8 105–115 (Springer, 2017).
- 802 22. Tward, D. *et al.* 3d mapping of serial histology sections with anomalies using a novel robust deformable registration algorithm. in *International workshop on multimodal brain image analysis* 162–173 (Springer, 2019).
- 803 23. Cahill, L. S. *et al.* Preparation of fixed mouse brains for MRI. *Neuroimage* **60**, 933–939 (2012).
- 804 24. Sunkin, S. M. *et al.* Allen brain atlas: An integrated spatio-temporal portal for exploring the central nervous system. *Nucleic acids research* **41**, D996–D1008 (2012).
- 805 25. Kim, Y. *et al.* Brain-wide maps reveal stereotyped cell-type-based cortical architecture and subcortical sexual dimorphism. *Cell* **171**, 456–469 (2017).
- 806 26. Fürth, D. *et al.* An interactive framework for whole-brain maps at cellular resolution. *Nat Neurosci* **21**, 139–149 (2018).

- 807 27. Li, Y. *et al.* mBrainAligner-web: A web server for cross-modal coherent registration
of whole mouse brains. *Bioinformatics* **38**, 4654–4655 (2022).
- 808 28. Puchades, M. A., Csucs, G., Ledergerber, D., Leergaard, T. B. & Bjaalie, J. G. Spatial
registration of serial microscopic brain images to three-dimensional reference atlases
with the QuickNII tool. *PloS one* **14**, e0216796 (2019).
- 809 29. Eastwood, B. S. *et al.* Whole mouse brain reconstruction and registration to a ref-
erence atlas with standard histochemical processing of coronal sections. *Journal of
Comparative Neurology* **527**, 2170–2178 (2019).
- 810 30. Ni, H. *et al.* A robust image registration interface for large volume brain atlas. *Sci
Rep* **10**, 2139 (2020).
- 811 31. Pallast, N. *et al.* Processing pipeline for atlas-based imaging data analysis of struc-
tural and functional mouse brain MRI (AIDAmri). *Front Neuroinform* **13**, 42 (2019).
- 812 32. Celestine, M., Nadkarni, N. A., Garin, C. M., Bougacha, S. & Dhenain, M. **Sammba-
MRI: A library for processing SmAll-MaMmal BrAin MRI data in python.** *Front
Neuroinform* **14**, 24 (2020).
- 813 33. Ioanas, H.-I., Marks, M., Zerbi, V., Yanik, M. F. & Rudin, M. **An optimized regis-
tration workflow and standard geometric space for small animal brain imaging.** *Neu-
roimage* **241**, 118386 (2021).
- 814 34. Perens, J. *et al.* Multimodal 3D mouse brain atlas framework with the skull-derived
coordinate system. *Neuroinformatics* **21**, 269–286 (2023).
- 815 35. Aggarwal, M., Zhang, J., Miller, M. I., Sidman, R. L. & Mori, S. Magnetic resonance
imaging and micro-computed tomography combined atlas of developing and adult
mouse brains for stereotaxic surgery. *Neuroscience* **162**, 1339–1350 (2009).
- 816 36. Goubran, M. *et al.* **Multimodal image registration and connectivity analysis for inte-
gration of connectomic data from microscopy to MRI.** *Nat Commun* **10**, 5504 (2019).
- 817 37. Chandrashekhar, V. *et al.* CloudReg: Automatic terabyte-scale cross-modal brain
volume registration. *Nature methods* **18**, 845–846 (2021).
- 818 38. Jin, M. *et al.* **SMART: An open-source extension of WholeBrain for intact mouse
brain registration and segmentation.** *eNeuro* **9**, (2022).

- 819 39. Negwer, M. *et al.* FriendlyClearMap: An optimized toolkit for mouse brain mapping
and analysis. *Gigascience* **12**, (2022).
- 820 40. Lin, W. *et al.* Whole-brain mapping of histaminergic projections in mouse brain.
Proceedings of the National Academy of Sciences **120**, e2216231120 (2023).
- 821 41. Zhang, M. *et al.* Spatially resolved cell atlas of the mouse primary motor cortex by
MERFISH. *Nature* **598**, 137–143 (2021).
- 822 42. Shi, H. *et al.* Spatial atlas of the mouse central nervous system at molecular resolution.
Nature **622**, 552–561 (2023).
- 823 43. Zhang, Y. *et al.* Reference-based cell type matching of in situ image-based spatial
transcriptomics data on primary visual cortex of mouse brain. *Scientific Reports* **13**,
9567 (2023).
- 824 44. Klein, S., Staring, M., Murphy, K., Viergever, M. A. & Pluim, J. P. W. Elastix: A
toolbox for intensity-based medical image registration. *IEEE Trans Med Imaging* **29**,
196–205 (2010).
- 825 45. Fedorov, A. *et al.* 3D slicer as an image computing platform for the quantitative
imaging network. *Magnetic resonance imaging* **30**, 1323–1341 (2012).
- 826 46. Tustison, N. J. *et al.* The ANTsX ecosystem for quantitative biological and medical
imaging. *Sci Rep* **11**, 9068 (2021).
- 827 47. Pagani, M., Damiano, M., Galbusera, A., Tsafaris, S. A. & Gozzi, A. Semi-automated
registration-based anatomical labelling, voxel based morphometry and cortical thick-
ness mapping of the mouse brain. *Journal of neuroscience methods* **267**, 62–73 (2016).
- 828 48. Anderson, R. J. *et al.* Small animal multivariate brain analysis (SAMBA) - a high
throughput pipeline with a validation framework. *Neuroinformatics* **17**, 451–472
(2019).
- 829 49. Allan Johnson, G. *et al.* Whole mouse brain connectomics. *Journal of Comparative
Neurology* **527**, 2146–2157 (2019).
- 830 50. Yao, Z. *et al.* A high-resolution transcriptomic and spatial atlas of cell types in the
whole mouse brain. *Nature* **624**, 317–332 (2023).

- 831 51. Avants, B. B., Epstein, C. L., Grossman, M. & Gee, J. C. [Symmetric diffeomorphic](#)
image registration with cross-correlation: Evaluating automated labeling of elderly
and neurodegenerative brain. *Med Image Anal* **12**, 26–41 (2008).
- 832 52. Tustison, N. J. *et al.* [N4ITK: Improved N3 bias correction](#). *IEEE Trans Med Imaging*
29, 1310–20 (2010).
- 833 53. Bajcsy, R. & Broit, C. Matching of deformed images. in *Sixth International Conference on Pattern Recognition (ICPR'82)* 351–353 (1982).
- 834 54. Bajcsy, R. & Kovacic, S. [Multiresolution elastic matching](#). *Computer Vision, Graphics, and Image Processing* **46**, 1–21 (1989).
- 835 55. Gee, J. C., Reivich, M. & Bajcsy, R. [Elastically deforming 3D atlas to match anatomical brain images](#). *J Comput Assist Tomogr* **17**, 225–36 (1993).
- 836 56. Klein, A. *et al.* [Evaluation of 14 nonlinear deformation algorithms applied to human brain MRI registration](#). *Neuroimage* **46**, 786–802 (2009).
- 837 57. Murphy, K. *et al.* [Evaluation of registration methods on thoracic CT: The EMPIRE10 challenge](#). *IEEE Trans Med Imaging* **30**, 1901–20 (2011).
- 838 58. Baheti, B. *et al.* [The brain tumor sequence registration challenge: Establishing correspondence between pre-operative and follow-up MRI scans of diffuse glioma patients](#). (2021).
- 839 59. Avants, B. B. *et al.* [The optimal template effect in hippocampus studies of diseased populations](#). *Neuroimage* **49**, 2457–66 (2010).
- 840 60. Avants, B. B., Tustison, N. J., Wu, J., Cook, P. A. & Gee, J. C. [An open source multivariate framework for n-tissue segmentation with evaluation on public data](#). *Neuroinformatics* **9**, 381–400 (2011).
- 841 61. Manjón, J. V., Coupé, P., Martí-Bonmatí, L., Collins, D. L. & Robles, M. [Adaptive non-local means denoising of MR images with spatially varying noise levels](#). *J Magn Reson Imaging* **31**, 192–203 (2010).
- 842 62. Wang, H. *et al.* [Multi-atlas segmentation with joint label fusion](#). *IEEE Trans Pattern Anal Mach Intell* **35**, 611–23 (2013).

- 843 63. Tustison, N. J. *et al.* Optimal symmetric multimodal templates and concatenated random forests for supervised brain tumor segmentation (simplified) with *ANTsR*. *Neuroinformatics* (2014) doi:[10.1007/s12021-014-9245-2](https://doi.org/10.1007/s12021-014-9245-2).
- 844 64. Tustison, N. J., Yang, Y. & Salerno, M. **Advanced normalization tools for cardiac motion correction**. in *Statistical atlases and computational models of the heart - imaging and modelling challenges* (eds. Camara, O. et al.) vol. 8896 3–12 (Springer International Publishing, 2015).
- 845 65. McCormick, M., Liu, X., Jomier, J., Marion, C. & Ibanez, L. **ITK: Enabling reproducible research and open science**. *Front Neuroinform* **8**, 13 (2014).
- 846 66. Beg, M. F., Miller, M. I., Trouvé, A. & Younes, L. **Computing large deformation metric mappings via geodesic flows of diffeomorphisms**. *International Journal of Computer Vision* **61**, 139–157 (2005).
- 847 67. Tustison, N. J. & Avants, B. B. **Explicit B-spline regularization in diffeomorphic image registration**. *Front Neuroinform* **7**, 39 (2013).
- 848 68. Hsu, L.-M. *et al.* CAMRI mouse brain MRI data.
- 849 69. Reshetnikov, V. *et al.* High-resolution MRI data of brain C57BL/6 and BTBR mice in three different anatomical views.
- 850 70. Rahman, N., Xu, K., Budde, M. D., Brown, A. & Baron, C. A. **A longitudinal microstructural MRI dataset in healthy C57Bl/6 mice at 9.4 tesla**. *Sci Data* **10**, 94 (2023).
- 851 71. Liu, J. *et al.* **Concordance of MERFISH spatial transcriptomics with bulk and single-cell RNA sequencing**. *Life Sci Alliance* **6**, (2023).
- 852 72. Stringer, C., Wang, T., Michaelos, M. & Pachitariu, M. **Cellpose: A generalist algorithm for cellular segmentation**. *Nat Methods* **18**, 100–106 (2021).
- 853 73. Jia, H., Yap, P.-T., Wu, G., Wang, Q. & Shen, D. **Intermediate templates guided groupwise registration of diffusion tensor images**. *NeuroImage* **54**, 928–939 (2011).
- 854 74. Tang, S., Fan, Y., Wu, G., Kim, M. & Shen, D. **RABBIT: Rapid alignment of brains by building intermediate templates**. *NeuroImage* **47**, 1277–1287 (2009).

- 855 75. Dewey, B. E., Carass, A., Blitz, A. M. & Prince, J. L. Efficient multi-atlas registration using an intermediate template image. in *Proceedings of SPIE—the international society for optical engineering* vol. 10137 (NIH Public Access, 2017).
- 856 76. Gong, H. *et al.* High-throughput dual-colour precision imaging for brain-wide connectome with cytoarchitectonic landmarks at the cellular level. *Nat Commun* **7**, 12142 (2016).
- 857 77. Wang, J. *et al.* Divergent projection patterns revealed by reconstruction of individual neurons in orbitofrontal cortex. *Neurosci Bull* **37**, 461–477 (2021).
- 858 78. Rotolo, T., Smallwood, P. M., Williams, J. & Nathans, J. Genetically-directed, cell type-specific sparse labeling for the analysis of neuronal morphology. *PLoS One* **3**, e4099 (2008).
- 859 79. Peng, H. *et al.* Morphological diversity of single neurons in molecularly defined cell types. *Nature* **598**, 174–181 (2021).
- 860 80. Chon, U., Vanselow, D. J., Cheng, K. C. & Kim, Y. Enhanced and unified anatomical labeling for a common mouse brain atlas. *Nat Commun* **10**, 5067 (2019).
- 861 81. Tasic, B. *et al.* Adult mouse cortical cell taxonomy revealed by single cell transcriptomics. *Nat Neurosci* **19**, 335–46 (2016).
- 862 82. Bergmann, E., Gofman, X., Kavushansky, A. & Kahn, I. Individual variability in functional connectivity architecture of the mouse brain. *Commun Biol* **3**, 738 (2020).
- 863 83. Billot, B. *et al.* SynthSeg: Segmentation of brain MRI scans of any contrast and resolution without retraining. *Med Image Anal* **86**, 102789 (2023).
- 864 84. Tustison, N. J. & Amini, A. A. Biventricular myocardial strains via nonrigid registration of anatomical NURBS model [corrected]. *IEEE Trans Med Imaging* **25**, 94–112 (2006).
- 865 85. Tustison, N. J. *et al.* Large-scale evaluation of ANTs and FreeSurfer cortical thickness measurements. *Neuroimage* **99**, 166–79 (2014).
- 866 86. Das, S. R., Avants, B. B., Grossman, M. & Gee, J. C. Registration based cortical thickness measurement. *Neuroimage* **45**, 867–79 (2009).

- 867 87. Tustison, N. J. *et al.* Longitudinal mapping of cortical thickness measurements: An Alzheimer's Disease Neuroimaging Initiative-based evaluation study. *J Alzheimers Dis* (2019) doi:[10.3233/JAD-190283](https://doi.org/10.3233/JAD-190283).
- 868 88. Grewal, J. S. *et al.* Brain gyration in wild and domestic canids: Has domestication changed the gyration index in domestic dogs? *J Comp Neurol* **528**, 3209–3228 (2020).
- 869 89. Avelino-de-Souza, K. *et al.* Anatomical and volumetric description of the guiana dolphin (*sotalia guianensis*) brain from an ultra-high-field magnetic resonance imaging. *Brain Struct Funct* (2024) doi:[10.1007/s00429-024-02789-1](https://doi.org/10.1007/s00429-024-02789-1).
- 870 90. Demirci, N., Hoffman, M. E. & Holland, M. A. Systematic cortical thickness and curvature patterns in primates. *Neuroimage* **278**, 120283 (2023).
- 871 91. Lerch, J. P. *et al.* Cortical thickness measured from MRI in the YAC128 mouse model of huntington's disease. *Neuroimage* **41**, 243–51 (2008).
- 872 92. Lee, J. *et al.* Automatic cortical thickness analysis on rodent brain. *Proc SPIE Int Soc Opt Eng* **7962**, 7962481–79624811 (2011).
- 873 93. Zöller, T., Attaai, A., Potru, P. S., Ruß, T. & Spittau, B. Aged mouse cortical microglia display an activation profile suggesting immunotolerogenic functions. *Int J Mol Sci* **19**, 706 (2018).
- 874 94. Avants, B. B. *et al.* The Insight ToolKit image registration framework. *Front Neuroinform* **8**, 44 (2014).
- 875 95. Avants, B. B. *et al.* A reproducible evaluation of ANTs similarity metric performance in brain image registration. *Neuroimage* **54**, 2033–44 (2011).
- 876 96. Nyúl, L. G., Udupa, J. K. & Zhang, X. New variants of a method of MRI scale standardization. *IEEE Trans Med Imaging* **19**, 143–50 (2000).
- 877 97. Falk, T. *et al.* U-net: Deep learning for cell counting, detection, and morphometry. *Nat Methods* **16**, 67–70 (2019).